International Journal of GEOMATE, Aug., 2021, Vol.21, Issue 84, pp.167-176
ISSN: 2186-2982 (P), 2186-2990 (O), Japan, DOI: https://doi.org/10.21660/2021.84.j2163
Geotechnique, Construction Materials and Environment

ASSESSING SHEAR-LAG EFFECT ON PULTRUDED FRP RODS BASED ON A NUMERICAL SIMULATION

*Nam Van Vo[1] and Isamu Yoshitake[1]

[1]Graduate School of Sciences and Technology for Innovation, Yamaguchi University, Japan.

*Corresponding Author, Received: 9 April 2021, Revised: 10 May 2021, Accepted: 13 June 2021

ABSTRACT: Fiber reinforced polymer rods fabricated from unidirectional fibers and a polymer matrix strengthen effectively reinforced concrete structures, such as the use in near-surface mounted systems. This study focused on aramid fiber reinforced polymer (AFRP) and analytically assessed the shear-lag effect that significantly affects the tensile capacity of the rod. A representative volume element model was employed for predicting the transversely isotropic properties of AFRP rods. In addition, a finite element simulation for the tension test model was performed to assess the shear-lag effect of an AFRP rod with various diameters. The study proposed a procedure for calculating the stress distribution in any cross-section of a fiber reinforced polymer rod. The simulation results agreed well with the previous experimental study. The findings clearly indicated the position of the failure section and the unequal tensile stress distribution in it. The study revealed that the shear-lag effect varied by the rod diameter affects the stress distribution at the failure section and the tensile capacity. The paper shows that the ultimate tensile capacity of any pultruded FRP rod can be predicted by the proposed method.

Keywords: Finite element analysis (FEA); AFRP rod; Pultrusion; Shear-lag, RVE.

1. INTRODUCTION

Fiber reinforced polymer (FRP) materials have been widely used in various engineering applications. The FRPs are combinations of different fiber types (e.g., carbon, glass, aramid, or basalt) with matrix materials such as epoxies or vinylesters. One of the significant features of the FRPs is high tensile strength. In reinforced concrete applications, three common shapes of the FRPs offered by manufacturers are sheets, cables (tendons), and rods [1]. The study particularly focuses on the tensile properties of the FRP rods made of fibers and a matrix by the pultrusion method.

The mechanical properties of FRP rods depend upon the characteristics of their constituent components, i.e., matrices and fibers. The rod dimensions should be considered for assessing the tensile capacity of FRP rods in addition to the other influencing factors such as fiber type, matrix, temperature, and environment. The tensile strengths of the FRP rods containing a similar fiber volume fraction were significantly decreased with increasing the rod diameter [2–5]. Some studies reported that the phenomenon was caused by the shear-lag effect [6,7], as shown in Fig.1. The shear-lag effect of composites materials implies the stress transfer between fibers and a matrix, or in laminate composites. The definition of "shear-lag effect" in this paper is only utilized to analyze unequal stress distribution in the cross-sections of the FRP rods pulled out of filling materials (mortar and resin) in near-surface mounted systems. The shear-lag effect is available in all kinds of pultruded FRP rods (glass, basalt, carbon, and aramid FRPs). The axial tensile stress is higher at the lateral surface and lower at the core of FRP rods. The shear stiffness plays a key role in the stress transfer. Many researchers also mentioned the shear-lag effect in their studies on the bond performance of FRP rods [8–12]. However, a reasonable procedure for predicting the axial tensile stress distribution in the cross-section has not been proposed yet. In addition, it is unclear how the transversely isotropic properties of FRP rods and such fibers (aramid and carbon) are collected and evaluated. Consequently, the behavior of FRP rods in the tensile models has been limited.

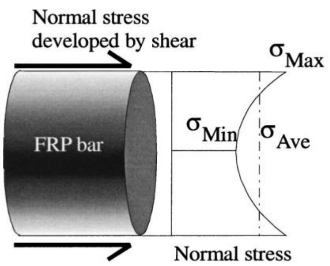

Fig.1 Shear-lag effect [7]

To quantify the shear-lag effect in detail, the present study employed two three-dimensional (3D) models. The models were representative volume element (RVE) and analysis models to predict mechanical properties and reveal the axial tensile stress distribution in the FRP rod, respectively. In addition, a technique called the sub-modeling method was used to enhance the accuracy of the results. The models in this study required the detailing mechanical properties of the fibers, matrix, and fiber volume fraction. The effect of transversely isotropic properties of fibers on the stiffness of FRP rods was considered. However, most of such information is the secret of manufacturers. The relevant information for this study was obtained from the previous investigation on aramid fiber reinforced polymer (AFRP) rods of 3-8 mm diameter under room temperature [5], which were made of aramid fibers and a vinylester resin. Hence, the present study mainly discussed the shear-lag effect of AFRP rods based on numerical simulations.

2. METHODOLOGY

2.1 Materials

The properties of FRP rods depend on the quality of constituting materials, fiber orientation, and volume fraction. Fig.2 shows the tensile properties of fibers, a matrix, and their composition. The tensile strengths of the fibers are significantly higher than that of the matrix. However, the ultimate tensile strain of the matrix is much higher than that of the fibers. The failure strain of an FRP composite is assumed to be the fiber ultimate strain.

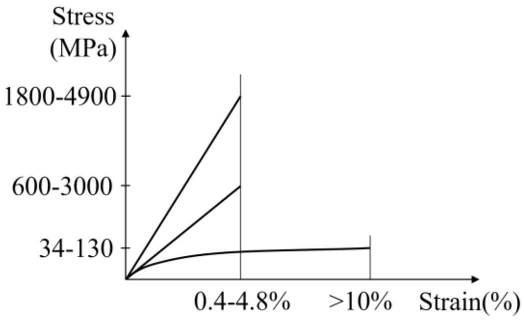

Fig.2 Stress-strain relationships of fibrous reinforcement and matrix [13]

This study focused on AFRP rods made of unidirectional fibers and a matrix by the pultrusion method. Both AFRP rods and aramid fibers exhibit transversely isotropic properties. Engineering elastic constants include Young's moduli (E_1, E_2= E_3), shear moduli (G_{12}= G_{13}, G_{23}), and Poisson's ratios ($\nu_{12}=\nu_{13}$, $\nu_{21}=\nu_{31}$, $\nu_{23}\neq\nu_{32}$). The transversely isotropic material follows restrictions on engineering constants in Eq. (1).

$$\frac{\nu_{ij}}{E_i} = \frac{\nu_{ji}}{E_j}$$
$$0 < \nu_{ij} < \sqrt{\frac{E_i}{E_j}};\ i,j = 1\ldots3; i \neq j \quad (1)$$
$$\varDelta = 1 - \nu_{12}\nu_{21} - \nu_{23}\nu_{32} - \nu_{31}\nu_{13} - 2\nu_{21}\nu_{32}\nu_{13}$$

Most of the material properties were collected from the study of Noritake *et al.* [5]. The information was listed in Table 1. However, Technora, a type of aramid fiber, is a transversely isotropic material. It requires more engineering constants to define the mechanical properties. The testing on a single fiber is a challenge because of the micro diameter. The transverse modulus E_2 was assumed from a transversely compressive test on the single Technora fiber [14]. Kalantar *et al.* [15] showed a nominal literature value of Poisson's ratio ν_{12}=0.35. However, this value is not appropriate in consideration of the significant difference between tensile stiffnesses in directions of 1 and 2. The shear modulus G_{12} and Poisson's ratios (ν_{12} and ν_{23}) were estimated from another aramid fiber Kevlar KM2 [16] having approximate material constants. The shear modulus G_{23} was calculated from the relationship $G_{23}=E_2/(1+\nu_{23})$.

2.2 Numerical Model

2.2.1 RVE model

FRPs are heterogeneous materials requiring many complicating tests to find all engineering elastic constants. A simple rule is to consider heterogeneous materials as homogeneous materials with approximate properties. This technique is called the homogeneous method using micromechanics models. Barbero [17] indicated advances in numerical homogenization using a 3D-FE model to estimate all engineering elastic constants. The effectiveness of the RVE model was confirmed in a previous study[18]. Fig.3 shows a hexagonal-microstructure RVE model employed in the present study. The model has transversely isotropic properties. Three parameters ($2a_1$, $2a_2$, $2a_3$) indicate the dimensions in a 3D space. The fiber direction aligns with the 1-axis. The relationship of three parameters is shown in Eq. (2) [17].

$$a_1 = a_2/4$$
$$a_3 = a_2 tan(60^0) \quad (2)$$
$$V_f = \frac{\pi d_f^2/2}{2a_2 2a_3}$$

where V_f and d_f are the volume fraction and diameter of the fiber, respectively.

Table 1 Properties of fiber and matrix [5]

Type	Tensile strength (MPa)	Tensile modulus (MPa)	Shear modulus (MPa)	Elongation (%)	Diameter (×10-3 mm)	Volume fraction (%)	Poisson's ratio
Technora fiber**	3500	E_1=74000 E_2=1590*	G_{12}=24400* G_{23}=641*	4.6	12	65	ν_{12}=0.60* ν_{23}=0.24*
Vinylester resin	90	3400	-	-	-	35	0.373

* These values were collected from other studies explained in section 2.1 Materials.
** The value i_{th}=1 in moduli E_i and Poisson's ratios ν_{ij} denotes the longitudinal direction of the fiber.

Eq. (3) [17] indicates the relationship between the average stress $\overline{\sigma}_\alpha$ and strain $\overline{\varepsilon}_\beta$ of the RVE model. Values are calculated over the total volume of the RVE model. The coefficients (α, β = 1– 6) are contracted notations to indicate six following components of stress and strain. $C_{\alpha\beta}$ is the stiffness tensor.

$$\overline{\sigma}_\alpha = C_{\alpha\beta}\overline{\varepsilon}_\beta \tag{3}$$

Luciano *et al.* [19] demonstrated the relationship between edge displacements and strains of the RVE model in Eq. (4). Values (u_i and ε_{ij}^0) are the applied displacement on each edge and applied strain of the RVE model, respectively. In addition, $2a_j\varepsilon_{ij}^0$ indicates the total displacement over length $2a_j$ to enforce a strain ε_{ij}^0. The theory assumes the continuity inside the RVE model. It means that there are no voids and cracks. The applied strain ε_{ij}^0 denotes the average strain of volume $\overline{\varepsilon}_\beta$. Equation (5) [17] shows the average strain in an RVE model.

$$\begin{aligned} u_i(a_1,x_2,x_3) - u_i(-a_1,x_2,x_3) &= 2a_1\varepsilon_{i1}^0 \\ u_i(x_1,a_2,x_3) - u_i(x_1,-a_2,x_3) &= 2a_2\varepsilon_{i2}^0 \\ u_i(x_1,x_2,a_3) - u_i(x_1,x_2,-a_3) &= 2a_3\varepsilon_{i3}^0 \end{aligned} \tag{4}$$

$$\overline{\varepsilon}_{ij} = \frac{1}{V}\int_V \varepsilon_{ij}dV = \varepsilon_{ij}^0 = \overline{\varepsilon}_\beta \tag{5}$$

where coefficients (i, j = 1–3) are contracted notations. The relationship between i, j and α, β follows Eq. (6) [17]:

$$\begin{aligned} \alpha,\beta &= i && \text{if } i = j \\ \alpha,\beta &= 9 - i - j && \text{if } i \neq j \end{aligned} \tag{6}$$

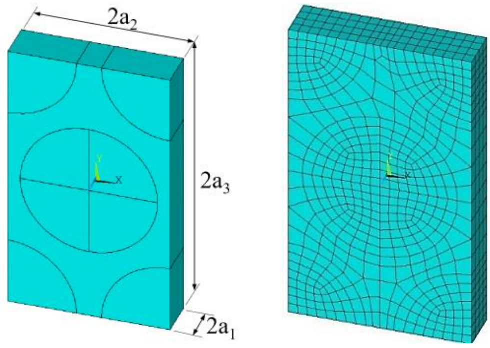

(a) (b)

Fig.3 RVE model in ANSYS: (a) Solid model, (b) FE model

By setting a unit value for the applied strain in Eq. (3) with β = 1–6, the RVE model is subjected to six components of strain. The computation is conducted with each of the cases. The stiffness tensor $C_{\alpha\beta}$ can be determined from Eq. (7) [17]. Barbero [17] reported a numerical simulation of the RVE model in Fig.3 to estimate all components of the stiffness tensor $C_{\alpha\beta}$. In addition, this study showed a procedure for calculating all engineering constants of the transversely isotropic material via tensor components in Eq. (8).

$$C_{\alpha\beta} = \overline{\sigma}_\alpha = \frac{1}{V}\int_V \sigma_\alpha(x_1,x_2,x_3)dV \quad \text{with } \overline{\varepsilon}_\beta = 1 \tag{7}$$

The dimensions of the RVE model in the present study were chosen by conditions in Eq. (2) to adapt to a fiber volume fraction of 65% (a_1=1.766, a_2=7.065, a_3=12.235). The RVE model was simulated using ANSYS software with the 3D solid element named SOLID186 defined by twenty nodes, as shown in Fig.3.

$$\begin{gathered} E_1 = C_{11} - 2C_{12}^2/(C_{22}+C_{23}) \\ E_2 = E_3 = [C_{11}(C_{22}+C_{23}) - 2C_{12}^2]\,(C_{22}-C_{23})/(C_{11}C_{22}-C_{12}^2) \\ G_{12} = G_{13} = C_{66} \\ G_{23} = C_{44} = (C_{22}-C_{23})/2 \\ \nu_{12} = \nu_{13} = C_{12}/(C_{22}+C_{23}) \\ \nu_{23} = (C_{11}C_{23}-C_{12}^2)/(C_{11}C_{22}-C_{12}^2) \end{gathered} \tag{8}$$

Materials in the RVE model were assumed to be linear. The engineering constants of the FRP rod computed from the RVE model were shown in Table 2.

Table 2 Results of FRP rod engineering constants

Tensile modulus (MPa)	Shear modulus (MPa)	Poisson's ratio
E_1 = 48806	G_{12} = 4717	ν_{12} = 0.489
E_2 = 2176	G_{23} = 807	ν_{23} = 0.349

2.2.2 Analysis model

a. Materials

Noritake *et al*. [5] showed that the tensile test was based on the bonding anchor system. The detailed properties of the filling material and steel tube were not reported. The Araldite epoxy resin (LY 556), with hardener HY 917 and accelerator DY 070 from Ciba Geigy, could be chosen as the filling material. De Kok *et al*. [20] showed the tensile test of epoxy LY 556 under room temperature (22^o C), as shown in Fig.4. The Young's modulus and strength of epoxy were evaluated from the curve. The steel tube properties were chosen from grade 310S products of MBM tubes [21]. Table 3 shows all engineering constants of the filling material and steel tube. Moreover, the transversely isotropic properties of the FRP rods (*d* = 3, 4, 6, 8 mm) were predicted in Table 2. The model used the y-axis as the tensile direction (the fiber direction). Young's modulus E_1 related to y-axis in the input information.

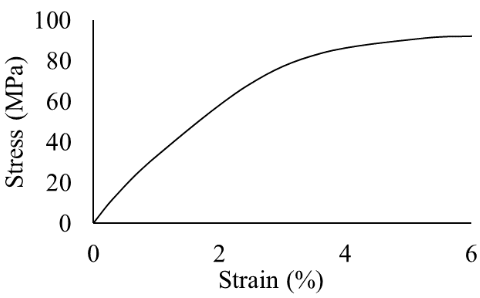

Fig.4 Tensile test of epoxy LY556 at 22^o C [20]

b. FE model

The numerical analysis model of a tensile test followed the standard ASTM D7205/D7205M−06 (2016) [22]. However, the simulation of a full model costs much computation. The analysis model is symmetric in tension. As shown in Fig.5 (a), using a half model can reduce a large number of elements. Unfortunately, the half model still costs much computing time. The half model uses the y-axis as the axis of rotational symmetry. In addition, the tensile load is also symmetrical. To optimize the computation, this study proposed a divided model based on the axisymmetric modeling method in ANSYS, as shown in Fig.5 (b). The divided model was split from the half model in Fig.5 (a) with an angle α. The value of α was calculated from the FRP rod radius and the element size 0.025 mm in Fig.5 (b). The divided model was called the global model adapting all details of the testing system.

Table 3 Material properties in the analysis model

Material	Properties
Epoxy LY 556 [20]	Young's modulus: E=3800 (MPa) Poisson's ratio: ν=0.37 Tensile strength: f_u = 92.2 (MPa)
Steel pipe grade 310S1 1/4 schedule 80S [21]	Young's modulus: E = 200000 (MPa) Poisson's ratio: ν = 0.30 Yield strength: f_y = 205 (MPa) Tensile strength: f_u = 515 (MPa)

The steel tube in the global model was used for transferring the tensile force from the applied load to the FRP rod. This study employed the NPS 1$^{1/4}$ - Schedule 80S tube from MBM tubes [21]. The tube characteristics follow American National Standard (ANSI B36.19 Stainless Steel Pipes), ASTM A 312/A 312M-01a. The steel tube sizes were recommended in the standard [22]. In addition, the steel tube thickness is enough to maintain a tensile stress that is lower than the yielding strength. Table 4 shows all FE model sizes of various FRP rods.

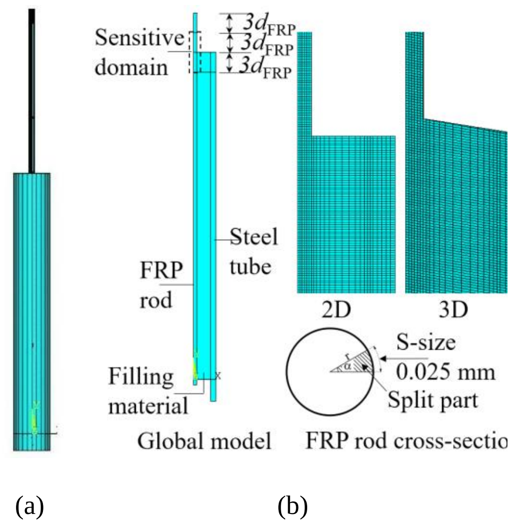

Fig.5 Analysis model in ANSYS: (a) half model; (b) divided model (global model)

Table 4 Sizes of the analysis model

Diameter of FRP bar (mm)	Outside diameter of the steel tube (mm)	Anchor length (L_a) (mm)	Free length (L) (mm)	Thickness of epoxy resin (mm)	Thickness of steel tubes (mm)
3				26.5	
4	42.2	300	380	24.5	4.85
6				20.5	
8				16.5	

The present study indicated that the shear lag only affects the domain (six times d_{FRP} of the free length and three times d_{FRP} of the bond length), as shown in Fig.5 (b). This finding helped to reduce the free length in the global model. Fig.6 presents the boundary conditions of the global model. The applied displacement on the steel tube in y-direction causes strains and stresses in the filling material and the FRP rod. The study defined an unbonded domain (5 mm) to avoid the large deformation of the vinylester resin at the interface. The stress distribution around the anchorage was complicated. Hence, a technique called the sub-modeling in ANSYS was employed for obtaining more accurate results in the sensitive domain in Figs.5 and 6. The sub-model only simulated the FRP rod in the sensitive domain (with a finer mesh) sized in the length of six times the rod diameter in Fig.6. The sub-model boundary conditions were interpolated from the global model results in Fig.5 (b). The global model and sub-model used a 3D-eight node solid element named SOLID185 in ANSYS. The simulation assumed the full bonding and continuity among materials.

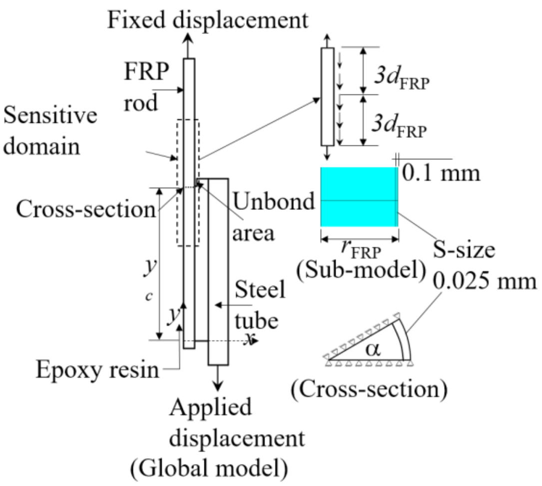

Fig.6 Boundary conditions of the analysis models

It is well known that simulation results are often affected by the element size. Table 5 shows all element sizes in the global model and sub-model. The global model was meshed with G-size at the sensitive domain and larger sizes at the others. The sub-model used a more refined mesh with S-size to enhance accuracy. The S-size=0.025 mm denoted the unchanged element size in area 0.1 mm close to the lateral surface of the FRP rod in the sub-model, as shown in Fig.6. The study employed three kinds of G-size (0.2, 0.25, and 0.5 mm) in the global model and three kinds of S-size (0.05 and 0.1 mm at inner domain, and an unchanged value of 0.025 mm at outer domain) in the sub-model. Six cases were conducted on the FRP rod (d=6 mm) to find the convergence value of ultimate tensile forces. The sub-model was considered as layers of elements following the radius direction. The averaging theory in Eq. (9) was proposed to find the average axial tensile stress in the y-axis in the cross-section.

$$\overline{\sigma}_j^y = \frac{1}{V}\int_V \sigma_i^y(x,y,z)dV = \frac{\sum_i \sigma_i^y V_i}{V_j} \qquad (9)$$

where σ_i^y is the axial tensile stress element i_{th} in layer j_{th}; $\overline{\sigma}_j^y$ is the average axial tensile stress of layer j_{th}. For example, Fig.7 (c) presents a cross-section of the FRP rod (d=6 mm) containing 33 layers of elements along the radius. The maximum applied displacement was determined at the value enforcing the ultimate stress σ_y, approximately 2245 MPa.

Table 5 Element sizes and ultimate tensile force results

D (mm)	G-size* (mm)	S-size* (mm)	Ultimate tensile force (kN)
6	0.50	0.10 & 0.025	54.81
	0.50	0.05 & 0.025	52.84
	0.25	0.10 & 0.025	52.55
	0.25	0.05 & 0.025	52.55
	0.20	0.10 & 0.025	51.97
	0.20	0.05 & 0.025	51.97

* G and S denote the global model and sub-model, respectively

3. RESULTS AND DISCUSSION

The global model in Fig.5 (b) was applied to simulate four types of diameters (d = 3, 4, 6, and 8 mm) under boundary conditions in Fig.6 and properties in Tables 2 and 3. The tensile stress distribution was presented in Fig.7. The cross-sections at the failure element and in the free length were called the failure section and the free section, respectively, as shown in Fig.7(b). The parameter y_c in Fig.6 denoted the cross-sectional position in the y-axis. The present study proposed a procedure following Eq. (9) for calculating the average tensile stress at each layer in a cross-section. For example, Table 6 reports the FRP rod results (d = 6 mm) at the failure section. The ultimate tensile force of the FRP rod was determined when the FRP rod was broken at the failure section.

$$P_u = \sigma_u^{rod} A \tag{10}$$

where P_u is the ultimate tensile force of the FRP rod. A and σ_u^{rod} are the area of the cross-section and the tensile strength of the FRP rod, respectively.

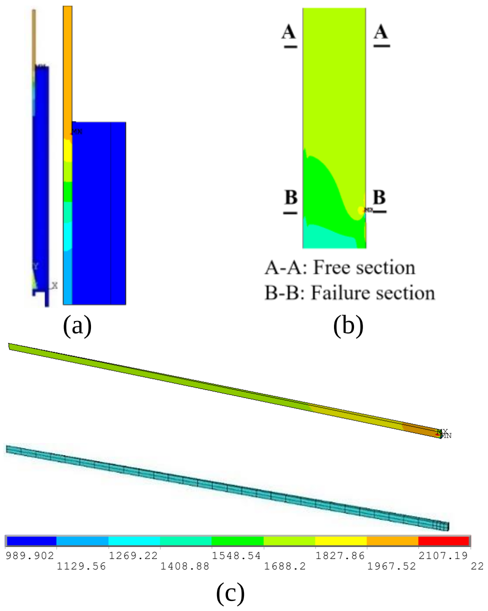

Fig.7 Tensile stress in y-direction of the FRP rod(d=6 mm): (a) around anchorage of the global model, (b) around the failure section of the sub-model, and (c) in the failure section of the sub-model

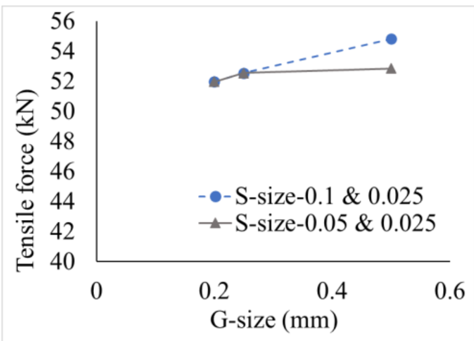

Fig.8 Tensile forces versus element sizes of the FRP rod (d=6 mm)

Table 5 and Fig.8 present the effect of the element size on the ultimate tensile force. Six cases of various element sizes were applied to find the ultimate tensile forces. The tensile force value converges at the G-size from 0.2 to 0.25 mm. and S-size from 0.05 to 0.1 mm in Fig.8. The element size affects the number of elements and computing time. Hence, the appropriate G-size and S-size are 0.25 and 0.1 mm, respectively. Four types of diameters were simulated with these element sizes. The S-size (0.025 mm) remains unchanged at the area close to the lateral surface of the FRP rod in all cases.

Table 6 Average tensile stress of each layer in the failure section (d = 6 mm)

Layer j_{th}	V_j (mm^3)	$\sum_i \sigma_i^y V_i$ (MPa.mm^3)	$\bar{\sigma}_y^j$ (MPa)
1	0.000001	0.00183	1746.87
2	0.000003	0.00553	1751.88
3	0.000005	0.00923	1754.13
4	0.000007	0.01292	1755.00
5	0.000009	0.01662	1755.99
6	0.000012	0.02033	1757.21
7	0.000014	0.02405	1758.71
8	0.000016	0.02777	1760.49
9	0.000018	0.03151	1762.57
10	0.000020	0.03526	1764.97
11	0.000022	0.03903	1767.71
12	0.000024	0.04281	1770.83
13	0.000026	0.04662	1774.36
14	0.000028	0.05045	1778.35
15	0.000030	0.05431	1782.84
16	0.000033	0.05821	1787.91
17	0.000035	0.06214	1793.64
18	0.000037	0.06612	1800.14
19	0.000039	0.07016	1807.53
20	0.000041	0.07425	1816.01
21	0.000043	0.07843	1825.80
22	0.000045	0.08269	1837.21
23	0.000047	0.08707	1850.70
24	0.000049	0.09158	1866.83
25	0.000051	0.09628	1886.56
26	0.000053	0.10118	1911.06
27	0.000055	0.10636	1942.50
28	0.000056	0.11180	1983.74
29	0.000057	0.11666	2031.04
30	0.000014	0.02958	2055.74
31	0.000014	0.02969	2073.41
32	0.000014	0.02908	2055.36
33	0.000014	0.02707	1966.70

3.1 Effect of Shear Lag

The shear-lag effect was reported in Figs.7, 9, and 10. Fig.7 shows the axial tensile stress distribution in the global model of FRP rod (d=6 mm) under a displacement u_y = 2.675 mm on the head of the steel tube. Fig.9 shows the tensile stress σ_y in three sections. In the failure section, the tensile stress is higher in the outer layers and lower in the inner ones. The stress distribution of the failure section in Fig.9 is similar to that in Fig.1. The failure section and free section positions are at y_c=295 mm and y_c=318 mm, respectively. The cross-section (y_c=296 mm) is the intermediate phase between the two above sections. The shear lag only affected the domain from y_c=295 to 297 mm. The failure element contains the nodal stress of 2245 MPa. However, the stress of the failure element interpolated from the integration point results was lower, approximately 2073 MPa The failure-section stress decreases from a maximum (approximately 2073 MPa in the outer elements) to a minimum (approximately 1747 MPa at the core), reduced by 16%. The tensile stress in the free section remains at an approximate value of 1858 MPa, reaching 82.8% of the tensile strength of the FRP material. The tensile stress in the free section denotes the FRP rod tensile strength σ_u^{rod} in Eq. (10). Hence, the tensile strength of the FRP rod is lower than that of the FRP material.

The theoretical ultimate tensile force of the FRP rod (*d*=6 mm) could reach the value of 63.44 kN, with a material tensile strength of 2245 MPa. The ultimate tensile force (52.55 kN) simulated in the present study is lower than that of the theory, just reaching 82.8%. However, the simulation result approximates the experimental value (53.13 kN) [5], with a deviation of 1.1 %. In addition, Noritake *et al*. [5] measured the axial tensile strain in the free length of the FRP rod (*d*=6 mm), about 3.7%. It is consistent with the simulated free-length strain of 3.8%, with a deviation of 2.7%. The maximum strain in the free length is lower than that of the FRP material (4.6%). This finding indicates that the failure section is out of the free length and close to the anchorage. These results confirm the accuracy of the present model. This phenomenon is similar to tensile testing results in previous studies [23–27]. In addition, Fig.10 (a) shows the existence of the shear-lag effect in the failure sections of various diameters. The results demonstrated a nonlinear relationship between the radius and the axial tensile stress.

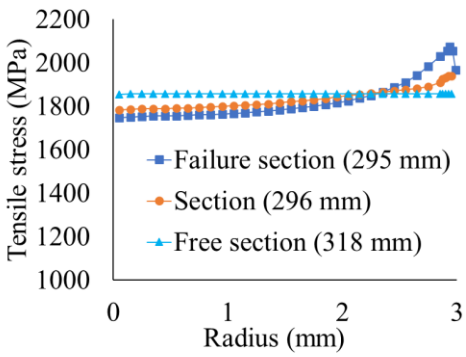

Fig.9 Axial tensile stress distribution in cross-sections of the FRP rod (*d*=6 mm)

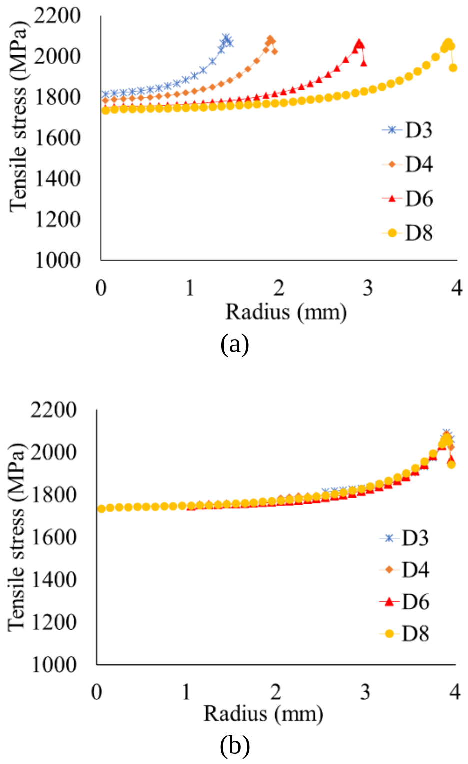

Fig.10 Distribution of axial tensile stress on the failure sections: (a) separated curves of diameters; (b) combined presentation based on the D8 curve

The shear-lag effect is one of the main reasons affecting the axial tensile stress distribution in the failure section of the FRP rod. It does not impact on the free length. The failure section is much more damaged than the free section. The present findings indicate that the FRP rod rupture must appear at the failure section. The shear-lag effect reduces the ultimate tensile capacity of FRP rods.

3.2 Effect of Rod Diameter

The stress distribution on the failure section is a function of the radius. Fig.10 (a) shows the separated curves of various FRP rods. The maximum stress at the outer elements of all diameters is similar to each other, approximately 2073 MPa. The study presented all curves on the D8 coordinate system to assess the shear-lag effect between diameters, as shown in Fig.10 (b). The findings show a similar rule of the stress decrease along the radius of four types of diameters. Two phases characterize the relationship at the failure section; namely, the axial tensile stress significantly decreases in the outer domain limited to 1 mm from the lateral surface of all diameters and then slightly goes down in the other domain. However, four outermost layers close to the lateral surface of the FRP rod show a dramatic fluctuation of the stress variation. The reason for this phenomenon is the significant effect of the shear-lag in this domain.

Table 7 Comparison of specified, experimental, and predicted results

Diameter (mm)	Ultimate tensile force P_u (kN)			Deviation (%)	
	Specified[a]	Experimental[a]	Predicted[b]	Spe-Pre[*]	Exp-Pre[*]
3	13.00	NA	13.66	5.1	NA
4	22.70	NA	23.86	5.1	NA
6	49.90	53.13	52.55	5.3	1.1
8	86.10	90.00	92.77	7.7	3.1

[a] The results in the previous study [5].
[b] The results in the present study.
[*] Pre: predicted; Spe: specified; Exp: experimental.
NA: not available.

Fig.11 shows the decrease of tensile strengths of four diameters from D3 to D8, with 6.8% for specified strength and 4.4% for predicted strength. The predicted strength follows the rule of the experimental and specified results of the previous study [5]. As considered in Fig. 10, the failure of FRP rods appears at the lateral surface containing higher stress. All FRP rods made of a similar volume fraction have a similar material tensile strength. FRP rods are ruptured when their tensile stress at the lateral surface reaches the material tensile strength. However, the diameter increase induces a decrease of tensile stress at the core of the FRP rod, as shown in Fig.10 (b). Consequently, the FRP rod is ruptured when tensile stress at the core is lower than that at the lateral surface. The present findings demonstrate that the diameter is one of the main factors affecting the tensile strength of the FRP rods.

3.3 Predicting the Ultimate Tensile Forces of FRP Rods

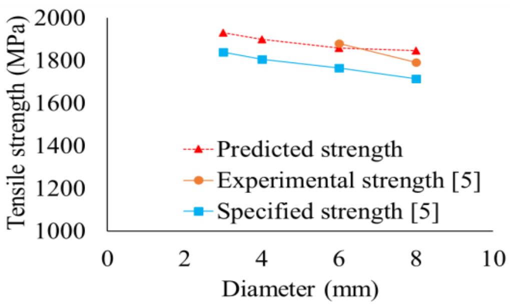

Fig.11Tensile strength decrease versus diameter

The study had shown a procedure to predict the ultimate tensile forces of the FRP rods (d=3, 4, 6, 8 mm). Table 7 shows the comparison of the specified, experimental, and predicted results. The deviation between the specified and predicted ultimate tensile forces varies from 5.1 to 7.7%. However, the specified values are always lower than the experimental ones because of the safety-factor consideration. Instead, the experimental results are more appropriate for the comparison. The predicted ultimate forces approximate to experimental ones, with the deviation from 1.1 to 3.1%. The present results are consistent with previous findings of Noritake *et al.* [5]. These findings confirm the effectiveness of the proposed model in predicting the ultimate tensile forces of the FRP rods. However, the limitation of the study is that the experimental results of FRP rods (d = 3 and 4 mm) in Table 7 were unavailable to compare with simulation ones.

4. CONCLUSIONS

The study aimed at determining the shear-lag effect in the pultruded FRP rods made of Technora fibers 65% and vinylester resin 35%. All material properties of FRP elements were predicted by the simulation using the RVE model. The analysis model was applied for four diameters (d = 3, 4, 6, 8 mm) of the AFRP rod. Based on the results and discussion, the conclusions are listed below:

- The present findings indicate the existence of the shear-lag effect and the failure section in the FRP rod by mechanical and numerical theory. It also clearly demonstrates the shear-lag phenomenon referenced in Firas *et al.* [6] and Achillides *et al.* [7]. The failure section is much more damaged than other cross-sections, and the FRP rod must be ruptured at this section.
- The shear-lag effect only causes the nonlinear distribution of the axial tensile stress in the cross-sections close to the anchorage. The stress profiles in the failure sections of all diameters include two phases: significantly decreasing in outermost layers and slightly declining in the other layers. The present study confirmed that the increase of the diameter induces the decrease of the tensile strength.
- The proposed model can be applicable in predicting the ultimate tensile capacity of any pultruded FRP rod. The deviations between the simulation and experimental results are unremarkable.

ACKNOWLEDGMENT

The authors would like to thank Editage (www.editage.jp) for English language editing.

REFERENCES

[1] ACI Committee 440, State-of-the-Art-Report on Fiber Reinforced Plastic (FRP) for Concrete Structures, ACI Struct. J., Vol. 92, Issue 5, 1995, pp. 627–628.

[2] Hughes Brothers, ASLAN TM 100, (2019). http://aslanfrp.com/resources/Aslan-100-GFRP-Rebar-data-sheet.pdf (accessed November 27, 2019).

[3] Structural technologies, V-WrapTM Glass FRP Rod, 1 (2018) 53. https://structuraltechnologies.com/wp-content/datasheet/TD_VWrap-Glass_FRP_Rod_2018-04-30.pdf (accessed November 27, 2019).

[4] Kodiak Rebar, Fiberglass Rebar (GFRP) Glass fiber reinforced polymer, (2019). https://www.fiberglassrebar.us/ (accessed November 27, 2019).

[5] Noritake K., Kakihara R., Kumagai S., and Mizutani J., Technora, an Aramid FRP Rod, Fiber-Reinforced-Plastic Reinf. Concr. Struct., , 4th ed , Vol. 1, Amsterdam, Ed. Nanni A., Elsevier Science, 1993, pp. 267–290.

[6] Firas S.A., Gilles F., Robert. L.R., Bond between carbon fibre-reinforced polymer (CFRP) bars and ultra high performance fibre reinforced concrete (UHPFRC): Experimental study, Constr. Build. Mater., Vol. 25, Issue 2, 2011, pp. 479–485.

[7] Achillides Z. and Pilakoutas K., Bond behavior of fiber reinforced polymer bars under direct pullout conditions, J. Compos. Constr., Vol. 8, No. 2, 2004, pp. 519–527.

[8] Kalamkarov A., Saha G., Rokkam S., Newhook J., and Georgiades A., Strain and deformation monitoring in infrastructure using embedded smart FRP reinforcements, Compos. Part B Eng., Vol. 36, Issue 5, 2005, pp. 455–467.

[9] Wang H., Sun X., Peng G., Luo Y., and Ying Q., Experimental study on bond behaviour between BFRP bar and engineered cementitious composite, Constr. Build. Mater., Vol. 95, 2015, pp. 448–456.

[10] Maranan G.B., Manalo A.C., Karunasena W., and Benmokrane B., Pullout behaviour of GFRP bars with anchor head in geopolymer concrete, Compos. Struct., Vol. 132, 2015, pp. 1113–1121.

[11] Li C., Gao D., Wang Y., and Tang J., Effect of high temperature on the bond performance between basalt fibre reinforced polymer (BFRP) bars and concrete, Constr. Build. Mater. Vol. 141, 2017, pp. 44–51.

[12] Benmokrane B., Manalo A., Bouhet J.C., and Mohamed K., R. Mathieu, Effects of Diameter on the Durability of Glass Fiber–Reinforced Polymer Bars Conditioned in Alkaline Solution, J. Compos. Constr. Vol. 21, Issue 5 , 2017, pp. 4017040 (1-12).

[13] Newhook J. and Svecova D., FRP Reinforced Materials, Reinforcing concrete structures with fibre reinforced polymers, Can. Netw. Centers Excell. Intell. Sens. Innov. Struct, Ed. Jaeger L., No. 3, 2007, pp. 4.1-4.12.

[14] Kawabata S., Measurement of the Transverse Mechanical Properties of High-performance Fibres, J. Text. Inst., Vol. 81, Issue 4, 1990, pp. 432–447.

[15] Kalantar J., Drzal L.T., and Grummon D.S., Structural Properties of Aramid Fibers and Their Influence on Fiber Adhesion, Controlled Interphases in Composite Materials, 1990, pp. 685–690.

[16] Cheng M., Chen W., Weerasooriya T., Mechanical Properties of Kevlar® KM2 Single Fiber, J. Eng. Mater. Technol., Vol. 127, Issue 2, 2005, pp. 197–203.

[17] Barbero E.J., Computational Micromechanics, Finite Element Analysis of Composite Materials Using ANSYS, 2nd, CRC Press, New York, 2014, pp. 151–178.

[18] Sun C.T. and Vaidya R.S., Prediction of composite properties from a representative volume element, Compos. Sci. Technol., Vol. 56, Issue 2, 1996, pp. 171–179.

[19] Luciano R., Sacco E., Variational methods for the homogenization of periodic heterogeneous media, Eur. J. Mech. A/Solids., Vol. 17, Issue 4, 1998, pp. 599–617.

[20] De Kok J.M.M. and Meijer H.E.H., Deformation, yield and fracture of unidirectional composites in transverse loading. 1. Influence of fibre volume fraction and test-temperature, Compos. Part A Appl. Sci. Manuf., Vol. 30, Issue 7, 1999, pp. 905–916.

[21] M.T. Pvt. Ltd, Pipe Dimenssion- Grade 310S, (n.d.). https://www.mbmtubes.com/pipe-dimensions.html (accessed December 2, 2020).

[22] ASTM D7205/D7205M-06, Standard Test Method for Tensile Properties of Fiber Reinforced Polymer Matrix Composite Bars, 2016.

[23] Benmokrane B., Zhang B., and Chennouf A., Tensile properties and pullout behaviour of AFRP and CFRP rods for grouted anchor applications, Constr. Build. Mater., Vol. 14, Issue 3, 2000, pp. 157–170.

[24] Kocaoz S., Samaranayake V.A., and Nanni A., Tensile characterization of glass FRP bars, Compos. Part B Eng., Vol. 36, Issue 2, 2005, pp. 127–134.
[25] Micelli F. and Nanni A., Tensile characterization of FRP rods for reinforced concrete structures, Mechanics of Composite Materials, Vol. 39, No. 4, 2003, pp. 445–463.
[26] Goldston M., Remennikov A., and Sheikh M.N., Experimental investigation of the behaviour of concrete beams reinforced with GFRP bars under static and impact loading, Eng. Struct., Vol. 113, 2016, pp. 220–232.
[27] Atutis E., Valivonis J., and Atutis M., Experimental study of concrete beams prestressed with basalt fiber reinforced polymers under cyclic load, Compos. Struct., Vol. 183, 2018, pp. 389–396.